Anisotropic signatures in the spin-boson model

F. Hartmann [1,*] S. Scali [2] and J. Anders [1,2]

[1]*University of Potsdam, Institute of Physics and Astronomy, Karl–Liebknecht–Str. 24–25, 14476 Potsdam, Germany*
[2]*Department of Physics and Astronomy, University of Exeter, Stocker Road, Exeter EX4 4QL, United Kingdom*

Thermal equilibrium properties of nanoscale systems deviate from standard macroscopic predictions due to non-negligible coupling to the environment. For anisotropic three-dimensional materials, we derive the mean force corrections to the equilibrium state of a classical spin vector. Specifically, we consider cubic, orthorhombic, and monoclinic symmetries, and compare their spin expectation values as a function of temperature. The results are valid at arbitrary coupling strength. We underpin the correctness of the mean force state by evidencing its match with the steady state of the simulated non-Markovian spin dynamics. The results show an explicit dependence on the symmetry of the confining material. In addition, some coupling symmetries show a spin-alignment transition at zero temperature. Finally, we quantify the work extraction potential of the mean force-generated inhomogeneities in the energy shells. Such inhomogeneities constitute a classical equivalent to quantum coherences.

I. INTRODUCTION

Standard thermodynamics assumes that the interaction between the system and the bath is negligible compared to the bare system's energy. Over the last years, much effort has been made to obtain a consistent thermodynamic theory of strongly coupled systems in the classical and quantum regime [1–10]. Here, the thermal equilibrium state is described by the mean force (Gibbs) state, which has been studied comprehensively in the classical and quantum regime for one-dimensional and isotropic three-dimensional interactions with the environment [11–15]. Recently, it has been shown that for the one-dimensional θ-angled spin-boson model, the quantum mean force state becomes precisely the classical mean force state in the large-spin limit [16]. This establishes the correspondence principle for an open system for the first time. Further, environment-induced coherences, so called energy-shell inhomogeneities, are found to be present in the classical mean force state [16,17].

Meanwhile, magnetic materials with anisotropic crystal structures have been studied in condensed matter physics and magnetism, such as the orthorhombic rare-earth compound $DyMnO_3$ [18–23]. Further examples are the Mn-doped monoclinic ZrO_2 compound [24] or monoclinic Fe_3Se_4 nanostructures [25–27]. Effects of the anisotropic crystal geometry lead to differences in the magnetization behavior with respect to temperature.

In this paper, we consider a three-dimensional classical spin-boson model, where the bath can be anisotropic. We give an analytical expression of the classical mean force (CMF) state and study the influence of cubic, orthorhombic and monoclinic crystalline symmetries. We show that the CMF state

is strongly dependent on the symmetry of the coupling. But for the cubic (isotropic) bath the CMF state reduces to the classical Gibbs (CG) state. Further, in the case of orthorhombic crystal symmetry, we find a spin-alignment transition at zero temperature. This results from a change in the potential minimum in the transition from weak to strong system-bath coupling. The observed classical spin-alignment transition shows similarities with the quantum phase transition in the one-dimensional quantum spin-boson model [28–33].

Lastly, anisotropic crystal symmetries lead to classical energy-shell inhomogeneities in the phase space density. These were recently linked to a work extraction potential by Smith *et al.* [17]. We show that not all anisotropic baths lead to energy-shell inhomogeneities even though they lead to mean force corrections. For the orthorhombic mean force state, we demonstrate that the maximal work extraction is a function of the bath temperature and coupling strength.

In order to answer the question of how different bath symmetries influence the equilibrium properties of a single spin, the paper is organized as follows. In Sec. II, we employ the spin-boson model to calculate the three-dimensional CMF state and use the Neumann principle to construct coupling tensors that represent different crystal symmetries. In Sec. III, we detail the mean force corrections caused by different crystal symmetries. For orthorhombic crystal symmetries, we observe a spin-alignment transition that we discuss in more detail in Sec. IV. Classical mean force states lead to energy-shell inhomogeneities, that we link to a work extraction potential in Sec. V. We conclude with a brief summary and discussion in Sec. VI.

II. SETUP

The spin-boson model is used in many different physical, chemical, and biological contexts [34–40]. For example, it is
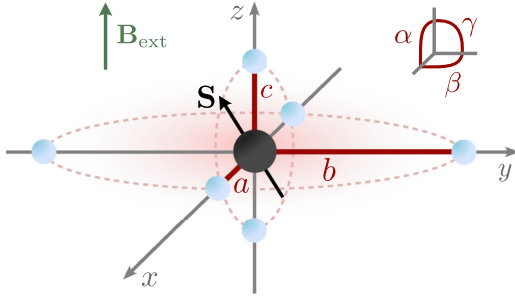
————
*hartmann3@uni-potsdam.de

FIG. 1. Sketch of a lattice giving rise to an anisotropic noise field. The spin (indicated in black) is surrounded by a bath of neighboring atoms (shown in light blue) forming an anisotropic lattice. Lattice vibrations (phonon excitations) at finite temperatures lead to an anisotropic noise field (red shade). Differences in lattice geometries result in different spin-bath interactions and thus to corrections to the spin's equilibrium state. The lattice parameters a, b, and c together with the angles α, β, and γ characterize different crystal classes, captured in the tensor $\mathcal{C}$. We set the external magnetic field $\mathbf{B}_{\mathrm{ext}}$ (green vector) to be aligned along the z direction.

adopted to describe the dissipation and decoherence effects in graphene [41] and to study the heat transfer in nonequilibrium situations [42]. Further, environment-induced quantum phase transitions between delocalized and localized states are observed in the spin-boson model [31,43] and it describes the physics of quantum emitters that are coupled to surface plasmons [44].

A. 3D spin-boson model

Here, we introduce the system, which is composed of a classical single spin vector $\mathbf{S}$ with length S_0, exposed to an external magnetic field $\mathbf{B}_{\mathrm{ext}} = (0, 0, B_z)$, with $\omega_{\mathrm{L}} = |\gamma| B_z$ being the Larmor frequency (see sketch in Fig. 1). The system Hamiltonian is given by

$$H_{\mathrm{S}} = -|\gamma| \mathbf{S} \cdot \mathbf{B}_{\mathrm{ext}} = -\omega_{\mathrm{L}} S_z. \tag{1}$$

The spin is embedded into a thermal bosonic bath. Even though we assume the bosonic bath to consist of phonons in a crystal lattice [45], one could also consider modes of an electromagnetic field [46]. We model the phonon modes by the Hamiltonian

$$H_{\mathrm{B}} = \frac{1}{2} \int_0^\infty d\omega \left(\mathbf{P}_\omega^2 + \omega^2 \mathbf{X}_\omega^2 \right), \tag{2}$$

where $\mathbf{P}_\omega$ and $\mathbf{X}_\omega$ are the three-dimensional phase space coordinates of the bath mode with frequency ω. The interaction between the system and the bath is assumed to be linear, which is sensible in most settings [11]. Hence, the interaction Hamiltonian is modelled as

$$H_{\mathrm{int}} = \mathbf{S} \cdot \int_0^\infty d\omega \, \mathcal{C}_\omega \mathbf{X}_\omega, \tag{3}$$

with $\mathcal{C}_\omega$ being the coupling tensor that determines the strength and the symmetry properties of the system-bath interaction. Unlike previous investigations establishing the link to the LLG equation [47] and the first open system quantum-classical correspondence [16], in this paper, we investigate

the physical implications of the (3×3) second rank coupling tensor $\mathcal{C}_\omega$ [45].

The total Hamiltonian of the combined system-bath compound is given by [16,47]

$$H_{\mathrm{tot}} = H_{\mathrm{S}} + H_{\mathrm{B}} + H_{\mathrm{int}}. \tag{4}$$

This Hamiltonian guides the dynamical evolution and the equilibrium features of the spin system interacting with a classical harmonic environment. The mean force state is generally defined as [11]

$$\tau_{\mathrm{MF}} := \mathrm{tr}_{\mathrm{B}}^{\mathrm{cl}}[\tau_{\mathrm{tot}}] = \mathrm{tr}_{\mathrm{B}}^{\mathrm{cl}}\left[\frac{e^{-\beta H_{\mathrm{tot}}}}{Z_{\mathrm{tot}}} \right]. \tag{5}$$

This is the reduced state of the global Gibbs state τ_{tot}, with the global partition function Z_{tot}, the inverse temperature $\beta = 1/k_{\mathrm{B}}T$, where k_{B} is the Boltzmann constant. Taking the partial trace in the classical setting $\mathrm{tr}_{\mathrm{B}}^{\mathrm{cl}}[\cdot]$ requires integrating over the bath degrees of freedom $(\mathbf{X}_\omega, \mathbf{P}_\omega)$ [16]. In the Appendix A, we show a detailed derivation and give the exact definitions of the classical partial trace of the bath and the spin system.

B. 3D classical mean force state (CMF)

Carrying out the trace over the bath, we derive the three-dimensional CMF state for arbitrary coupling strengths,

$$\tau_{\mathrm{MF}} = \frac{1}{\tilde{Z}_{\mathrm{S}}^{\mathrm{cl}}} e^{-\beta \left(H_{\mathrm{S}} - \frac{1}{2} \int_0^\infty d\omega \left(\mathbf{S}^{\mathrm{T}} \mathcal{C}_\omega \mathcal{C}_\omega^{\mathrm{T}} \mathbf{S} \right)/\omega^2 \right)}, \tag{6}$$

with $\tilde{Z}_{\mathrm{S}}^{\mathrm{cl}} = \mathrm{tr}_{\mathrm{S}}^{\mathrm{cl}}[\exp{-\beta(H_{\mathrm{S}} - \frac{1}{2} \int_0^\infty d\omega (\mathbf{S}^{\mathrm{T}} \mathcal{C}_\omega \mathcal{C}_\omega^{\mathrm{T}} \mathbf{S})/\omega^2)}]$ being the spin's CMF partition function. This is the first result of the paper and is an upgrade of the one-dimensional CMF state discussed in [16]. Our result is valid for any three-dimensional bath symmetry and all coupling strengths. It remains an open task to find a closed expression for the *quantum* mean force state for all coupling symmetries and coupling strengths [11,14,15].

From here onwards we will assume that the frequency dependence given by the spectral density J_ω is isotropic,

$$\mathcal{C}_\omega = \sqrt{2\omega J_\omega} \cdot \mathcal{C}. \tag{7}$$

But the overall strength of coupling can vary in different spatial directions, which is set by the elements of the tensor $\mathcal{C}$ (Sec. II C). In what follows, we assume that the spectral density of the lattice vibrations is of Lorentzian form $J_\omega = (A\Gamma\omega)/(\pi(\omega_0^2 - \omega^2)^2 + \pi\Gamma^2\omega^2)$. This is a reasonable assumption thanks to the bosonic spectral density J_ω being proportional to the phononic density of states D_ω, i.e., $J_\omega\omega \propto D_\omega$. Note that Lorentzian shaped spectral densities are a good choice to describe experimentally measured D_ω [45]. Furthermore, a Lorentzian spectral density has the advantage to lead to a closed set of differential equations when simulating the spin dynamics [16,47]. Under these assumptions, the frequency integral in the exponent of Eq. (6) then simplifies to the reorganization energy $Q = A/(2\omega_0^2)$. While the dynamics is governed by the peak width Γ, the eventual equilibrium state only depends on the resonant frequency ω_0 and the spin-bath coupling strength A [47]. Further, we rename the spin-matrix product $\mathbf{S}^{\mathrm{T}} \mathcal{C}\mathcal{C}^{\mathrm{T}} \mathbf{S} = \tilde{S}^2$ such that the CMF state
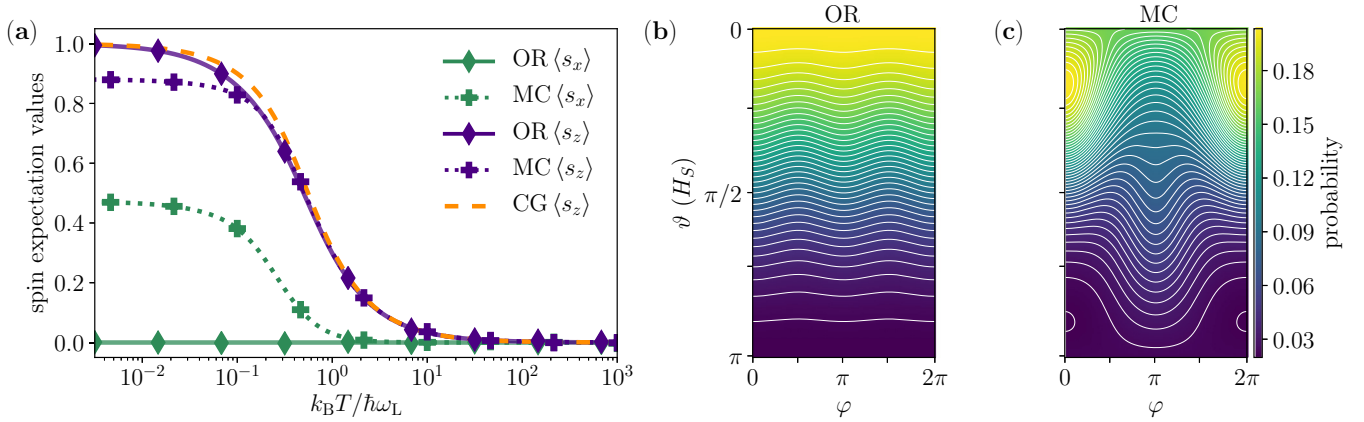
FIG. 2. CMF results for the orthorhombic and the monoclinic symmetry. Expectation values of the orthorhombic CMF state (OR, purple solid) and the monoclinic CMF state (MC, purple dotted) (a). We observe deviation from the CG state (orange dashed) in $\langle s_z \rangle$ ($s_z = S_z/S_0$) for both symmetries, and a nonzero expectation value $\langle s_x \rangle$ ($s_x = S_x/S_0$) for the monoclinic CMF state (green-dotted line). The results are supported by the corresponding dynamical CSS calculations (markers). The cubic CMF state is identical to the CG state (orange dashed). In (b), we show the phase space distribution of the orthorhombic CMF state, and in (c) of the monoclinic CMF state. The white lines indicate shells of equal probability. One sees that τ_{MF} is an inhomogeneous distribution over the energy shells of H_S for the orthorhombic and monoclinic symmetry, i.e., the white lines are not constant along φ. The expectation values and distributions are plotted for a temperature of $k_B T = \hbar \omega_L$, a reorganization energy of $Q = 2.5 \, \omega_L \hbar^{-1}$, and a spin length of $S_0 = \hbar$.

simplifies to [16]

$$\tau_{\mathrm{MF}}(\vartheta, \varphi) = \frac{1}{\tilde{Z}_S^{\mathrm{cl}}} e^{-\beta(H_S - Q\tilde{S}^2)}. \tag{8}$$

This $\tau_{\mathrm{MF}}(\vartheta, \varphi)$ is a distribution given in terms of the angles of the spherical coordinates (ϑ, φ), where $\mathbf{S} = S_0(\sin\vartheta\cos\varphi, \sin\vartheta\sin\varphi, \cos\vartheta)$ for a fixed spin length S_0.

The CMF state is postulated to be the thermal equilibrium state of a spin in contact with a bath, i.e., the dynamical classical steady state (CSS) in the long-time limit. While the correspondence of the CMF state and the CSS is proven in the weak-coupling limit [48] and the ultrastrong coupling regime [8] of quantum systems, there remain some open questions about the formal proof that this is valid for all coupling strengths and coupling symmetries [11,15].

Here, we demonstrate that the dynamics of a classical spin converges to the CMF state for classical noise, arbitrary coupling strength, and especially, any crystalline coupling symmetry, see Fig. 2(a). We do this by numerically solving the spin dynamics equations with the analytical and numerical methods detailed in Refs. [47,49]. These methods allow us to calculate the first- and higher-order moments of the spin components $s_i = S_i/S_0$ for $i = x, y, z$. For the spin vector rotating on the sphere the expectation values $\langle s_i \rangle$ are the most informative as they determine the equilibrium orientation inside the sphere. We find that the CMF expectation values and the CSS expectation values match, see Fig. 2(a). Higher moments, i.e., $\langle s_i^2 \rangle$ and $\langle s_i s_j \rangle$ for $i, j = x, y, z$, are also evaluated and found to match, see Appendix C.

C. Crystal symmetries

Coupling the spin to a harmonic bath that reflects the symmetry of the confining material requires knowledge about the coupling tensors $\mathcal{C}$. The specific form of the coupling tensor can be deduced from the Neumann principle [50,51].

The Neumann principle arises from symmetry considerations and connects the structure of a given crystal with its physical properties [50,52,53]. As a result, the coupling tensor must exhibit the same symmetry as the crystal it describes. This leads to the intuitive observation that, for crystals with more symmetries, the number of independent tensor components decreases. In general, the Neumann principle only determines the minimum number of symmetries of the coupling tensor. The specific form of the tensors that arise from the Neumann principle are discussed in the following by their contribution to the CMF state.

So far, we solely discussed the coupling tensor $\mathcal{C}$; however, we observe that, in Eq. (8), the symmetric product $\mathcal{C}\mathcal{C}^T$ is responsible for the mean force corrections. We restrict the product of the matrices $\mathcal{C}\mathcal{C}^T$ to follow the Neumann principle. In what follows, we refer to the components of $\mathcal{C}\mathcal{C}^T$ as

$$\mathcal{C}\mathcal{C}^T = \begin{pmatrix} c_{11} & c_{12} & c_{13} \\ c_{12} & c_{22} & c_{23} \\ c_{13} & c_{23} & c_{33} \end{pmatrix}. \tag{9}$$

Here, $\mathcal{C}\mathcal{C}^T$ is a symmetric, positive-definite tensor.

Different crystal classes are additionally characterized via their lattice parameters a, b, c, and the angles α, β, γ, as indicated in Fig. 1.

III. ANISOTROPIC MEAN FORCE CORRECTIONS

In this section, we summarize the effects that a three-dimensional bath with a given lattice structure has on the CMF state of the spin. In detail, we discuss cubic, orthorhombic, and monoclinic crystal symmetries. For comparability of the different crystal symmetries we always set the trace of the diagonalized property tensor to unity, i.e., $\mathrm{tr}[\mathcal{C}\mathcal{C}^T] = 1$.

A. Cubic

A cubic crystal symmetry, i.e., $\alpha = \beta = \gamma = 90°$ and $a = b = c$, results via the Neumann principle in an isotropic harmonic bath, i.e., the property tensor simplifies to $\mathcal{C}\mathcal{C}^{\mathrm{T}} = (1/3)\mathbb{1}_3$. It follows directly from the isotropy of the bath that the classical mean force state reduces to the classical Gibbs (CG) state, $\tau_{\mathrm{MF}}^{\mathrm{cubic}} = \tau_{\mathrm{Gibbs}} = e^{-\beta H_S}/\mathrm{tr}^{\mathrm{cl}}[e^{-\beta H_S}]$, since $\tilde{S}^2 = (1/3)S_0^2$ is constant and independent of (ϑ, φ). Thus, we observe that classical isotropic three-dimensional noise leaves the Gibbs state invariant with respect to any system-bath coupling strength Q.

Before we proceed with analyzing the CMF states for noncubic bath symmetries, we briefly remark on the quantum case, which will be the subject of future investigations. Firstly, in contrast to the classical cubic case discussed above, the quantum mean-force (QMF) state for cubic bath symmetry *does* show significant deviations from the corresponding quantum Gibbs state [54]. These deviations can be attributed to increased system-bath entanglement, i.e., the fact that the cubic CMF reduces to the CG is a purely classical phenomenon. Secondly, Ref. [16] proved the quantum-classical correspondence for MF states of a spin coupled to a bath in one arbitrary direction θ. But a similar proof for quantum systems coupled to three-dimensional baths, with either cubic or anisotropic symmetries, is so far missing.

Given the unsolved complexities of the three-dimensional quantum problem, we here proceed with mapping out the properties of the CMF for different three-dimensional symmetries.

B. Orthorhombic (OR)

Orthorhombic crystal symmetries have the following features: $a \neq b \neq c$ and $\alpha = \beta = \gamma = 90°$. This breaks the isotropy of the cubic crystal in the sense that neighboring atoms have different separations along orthogonal spatial directions. Hence, the property tensor of the coupling function has only diagonal elements. As an example, in Fig. 2, we choose $c_{11} = 0.40$, $c_{22} = 0.35$, $c_{33} = 0.25$ and the reorganization energy in the strong coupling regime with $Q = 2.5\,\omega_{\mathrm{L}}\hbar^{-1}$ [16].

The spin expectation values in the x and y directions are $\langle s_x \rangle = \langle s_y \rangle = 0$, identical to those of the CG state. This arises because the applied noise is invariant under rotation by $\varphi = \pi$ around the z axis. On the other hand, the expectation value $\langle s_z \rangle$ for the CMF state slightly deviates from the one corresponding to the CG state for most temperatures. But for $T \to 0\,\mathrm{K}$ both reach $\langle s_z \rangle = 1.0$, see Fig. 2(a).

For higher coupling strengths, e.g., $Q = 10\,\omega_{\mathrm{L}}\hbar^{-1}$, we observe a bump in the expectation value, as displayed in Appendix B. In many-body systems, such bumpy magnetization vs temperature measurements are encountered in materials that show a phase transition to anti–ferromagnetic ordering [18–21,23]. In Appendix B, we plot the temperature-dependent magnetization experiment of an orthorhombic DyMnO$_3$ single crystal from Ref. [18] together with the bumpy expectation value of the orthorhombic CMF state.

In Fig. 2(b), we show the CMF phase space distribution in the case of the OR symmetry. The contour white lines indicate shells of constant probability. Deviations from the CG state

are obvious, since τ_{Gibbs} would have straight parametric lines, i.e., no φ dependence. In contrast, for $\tau_{\mathrm{MF}}^{\mathrm{OR}}$ a teeth-like pattern is formed. It arises from the fact that $c_{11} > c_{22}$, and therefore, the spin components along the positive and negative x direction ($\varphi = 0, \pi$) are weighted stronger than the components along the y direction.

C. Monoclinic (MC)

Many features of classical mean force corrections are already observed by considering the orthorhombic crystal symmetry. However, by coupling to a monoclinic bath, further properties are discovered. In general, a monoclinic crystal structure is characterised via $a \neq b \neq c$ and $\alpha = \beta = 90° \neq \gamma$. This leads to a coupling tensor in Eq. (9) where we set the off-diagonal element $c_{13} \neq 0$ and fix the diagonal elements as for the orthorhombic symmetry. This geometrically corresponds to rotating the neighboring atoms in the $\pm x$ direction towards the z axis. It leads to a correction in the CMF state, i.e., $\tilde{S}^2 = c_{11}S_x^2 + c_{22}S_y^2 + c_{33}S_z^2 + 2c_{13}S_xS_z$, which has a cross-term of the spin components $S_xS_z \propto \cos\varphi \sin\vartheta \cos\vartheta$. This leads to a broken rotational invariance. We observe a CMF phase space distribution [Fig. 2(c)] that has a maximum rotated away from the positive z direction, towards the positive x direction. Further, along the negative x direction there is an increased probability to find the spin with a negative S_z component. This also leads to a nonzero expectation value $\langle s_x \rangle \neq 0$ for small temperatures $k_{\mathrm{B}}T/\hbar\omega_{\mathrm{L}} < 1$ [see Fig. 2(a)].

We conclude that the equilibrium properties of a classical spin vector drastically change when it is anisotropically coupled to a three-dimensional bath. In fact, its equilibrium features are highly dependent on the coupling strength, the temperature, and the crystal symmetry, i.e., the coupling tensor $\mathcal{C}\mathcal{C}^{\mathrm{T}}$.

IV. SPIN-ALIGNMENT TRANSITION

We want to study the classical spin expectation value $\langle s_z \rangle$ at zero temperature while increasing Q. Figure 3 shows the numerically calculated expectation values for the cubic, orthorhombic, and monoclinic symmetry at $T = 0\,\mathrm{K}$. For the three-dimensional orthorhombic CMF state (OR), we observe a spin-alignment transition, where the expectation value at a critical coupling strength $Q_{\mathrm{crit}}^{\mathrm{OR}}$ abruptly reduces from $\langle s_z \rangle = 1$ to $\langle s_z \rangle = 0$. The transition is characterized by minimizing the energy $H_{\mathrm{MF}}^{\mathrm{OR}}(\vartheta, \varphi) = H_S - Q\tilde{S}^2$, where we observe a repositioning of the energetic potential minimum,

$$\vartheta_{\min}^{\mathrm{OR}} = \begin{cases} 0 & y < 1, \\ \arccos\left(\frac{1}{y}\right) & y \geqslant 1, \end{cases} \tag{10}$$

with $y = Q/Q_{\mathrm{crit}}^{\mathrm{OR}}$ for $c_{11} > c_{33}$. The critical coupling strength is given by $Q_{\mathrm{crit}}^{\mathrm{OR}} = \omega_{\mathrm{L}}/(2(c_{11} - c_{33})S_0)$, as indicated in Fig. 3 by the grey-dashed vertical line. The azimuthal angle $\varphi_{\min}$ of the energetic potential minimum becomes $\varphi_{\min} = 0, \pi$ for $y \geqslant 1$. In other words, the energetic potential minimum becomes degenerate for coupling strengths larger than $Q_{\mathrm{crit}}^{\mathrm{OR}}$. In the zero-temperature limit, $\beta \to \infty$, the orthorhombic
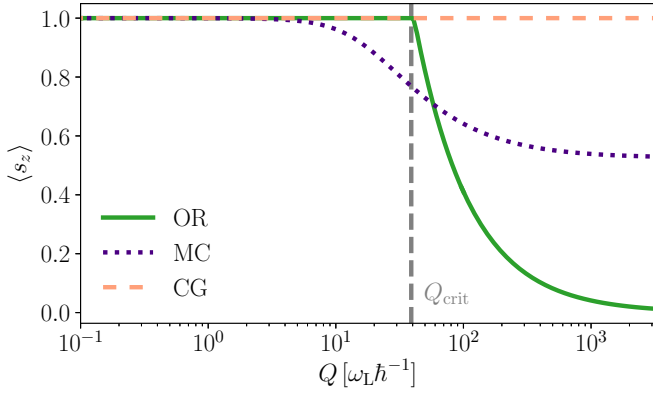
FIG. 3. Spin-alignment transition. s_z expectation value for the classical 3D spin-boson model for orthorhombic (OR, green solid) and monoclinic (MC, purple dotted) crystal symmetry at $T \to 0\,\mathrm{K}$ over coupling strength Q. The standard Gibbs state (orange dashed) is of course independent of Q. The vertical grey-dashed line indicates the critical coupling strength $Q_{\mathrm{crit}}^{\mathrm{OR}}$ at which the transition occurs in the orthorhombic CMF state. At $Q_{\mathrm{crit}}^{\mathrm{OR}}$ the most probable alignment of the spin changes from along the z axis towards the $\pm x$ axes. In contrast, the monoclinic expectation value reduces continuously to a finite expectation value $\langle s_z \rangle > 0$. All other parameters are as in Fig. 2.

expectation value is

$$\langle s_z \rangle_{\beta \to \infty} = \begin{cases} 1 & Q < Q_{\mathrm{crit}}^{\mathrm{OR}}, \\ Q_{\mathrm{crit}}^{\mathrm{OR}}/Q & Q \geqslant Q_{\mathrm{crit}}^{\mathrm{OR}}. \end{cases} \quad (11)$$

It is clear that the first derivative of (11) with respect to Q is discontinuous at $Q_{\mathrm{crit}}^{\mathrm{OR}}$, and the expectation value $\langle s_z \rangle_{\beta \to \infty}$ changes quickly from 1 to 0 for increasing Q. At the critical coupling strength it becomes energetically more convenient for the classical spin vector **S** to align along the x axis, with a consequent zero expectation value along the z direction, $\langle s_z \rangle = 0$. We note that this spin-alignment transition of a classical spin vector resembles the well-known quantum phase transition in the one-dimensional quantum spin-boson model [28–33,55]. This raises the question how the quantum phase transition is influenced by three-dimensional anisotropic baths in the quantum spin-boson model. This could be studied with the recently developed FP–HEOM approach, which is robust at zero temperature [56]. In contrast to the OR case, the monoclinic CMF state (MC) shows a smooth transition from $\langle s_z \rangle = 1$ to a finite value $\langle s_z \rangle > 0$ for increasing Q (see Fig. 3).

We conclude that the observed classical spin-alignment transition at zero temperature is highly dependent on the anisotropy of the system-bath coupling.

V. WORK EXTRACTION POTENTIAL

CMF corrections in the presence of anisotropic system-bath coupling can introduce energy-shell inhomogeneities [16], see Figs. 2(b) and 2(c). Recently Smith *et al.* [17] showed that classical inhomogeneities are equivalent to quantum coherences as a thermodynamic resource for work extraction [57]. Here, we link CMF states with anisotropic coupling to such a work extraction potential. Similar to the idea of extracting work from quantum coherences by altering the state with coherences to a state without coherences, one can extract

work from classical distributions by removing energy-shell inhomogeneities [17]. The energy shells are latitude circles, described by $H_{\mathrm{S}}(\vartheta)$, where the spin phase space is a sphere with radius S_0. The maximal work extraction is given by

$$\mathcal{W} = \beta^{-1}(S[\mathrm{diag}\,\tau_{\mathrm{MF}}(\vartheta)] - S[\tau_{\mathrm{MF}}(\vartheta, \varphi)]), \quad (12)$$

where, as before, $\tau_{\mathrm{MF}}(\vartheta, \varphi)$ is the CMF state, which may host energy-shell inhomogeneities, and $\mathrm{diag}\,\tau_{\mathrm{MF}}(\vartheta) = \int dE\, \eta(E)\, \omega_E(\vartheta, \varphi)$ defines the homogeneous distribution. Here, $\eta(E)$ is the distribution of energies of a phase space density $\rho(\Gamma)$ and $\omega_E(\cdot)$ is the classical microcanonical density. In addition, $S[\rho]$ refers to the Shannon entropy of a probability distribution ρ.

Following [17], we calculate the homogeneous distribution of the orthorhombic CMF state,

$$\mathrm{diag}\,\tau_{\mathrm{MF}}^{\mathrm{OR}}(\vartheta) = \frac{1}{\tilde{Z}_{\mathrm{S}}^{\mathrm{cl}}} \exp\left[-\beta\left(H_{\mathrm{S}} - QS_0^2 F(\vartheta)\right)\right]$$
$$\times \mathrm{I}_0\left[\frac{1}{2}\beta QS_0^2(c_{11} - c_{22})\sin^2\vartheta\right], \quad (13)$$

where $F(\vartheta) = \frac{1}{2}\sin^2\vartheta(c_{11} + c_{22}) - c_{33}\cos^2\vartheta$, and $\mathrm{I}_0(x)$ is the modified Bessel function of the first kind. A detailed derivation is given in Appendix D. Equation (13) is solely dependent on ϑ and, hence, is homogeneous in the energy shells $H_{\mathrm{S}}(\vartheta)$. In order to calculate the classical work potential $\mathcal{W}$, one needs a coarse-grained phase space distribution. The probability of the kth cell is given by $p_k = \int_{k^{\mathrm{th}}\,\mathrm{cell}} d\Omega\,\tau_{\mathrm{MF}}(\vartheta, \varphi)$ and $0 \leqslant p_k \leqslant 1$. Hence, the entropy in Eq. (12) is calculated via

$$S[\rho] = -\sum_k p_k \ln p_k, \quad (14)$$

for which $S[\rho] \geqslant 0$.

We want to compare the work potential of the orthorhombic case to that of other crystal symmetries. For example, the CMF state $\tau_{\mathrm{MF}}^{\mathrm{UA}}(\vartheta) \propto \exp[-\beta(H_{\mathrm{S}} - QS_0^2(c_{11}\sin^2\vartheta + c_{33}\cos^2\vartheta)]$, is for coupling to the bath with uniaxial (UA) symmetry. For this symmetry, $a = b \neq c$ and $\alpha = \beta = \gamma = 90°$, and the nontrivial elements in the tensor $\mathcal{C}\mathcal{C}^{\mathrm{T}}$ [Eq. (9)] are $c_{11} = c_{22} \neq c_{33}$. Even though the UA crystal symmetry introduces mean force corrections, the CMF state $\tau_{\mathrm{MF}}^{\mathrm{UA}}(\vartheta)$ has no energy-shell inhomogeneities, since it exclusively depends on ϑ. We can also view Eq. (12), as a measure of how inhomogeneous a given CMF state is for different system-bath symmetries, coupling strengths, and temperatures.

In Fig. 4, we compare the work extraction potential $\mathcal{W}$ for different crystal symmetries. As expected, the cubic crystal symmetry leads to $\mathcal{W} = 0$ (orange-dashed line). The same is observed for the uniaxial CMF state (blue-dotted line), since its mean force corrections do not host energy-shell inhomogeneities. But for the orthorhombic crystal symmetry a nonzero potential arises due to $\mathrm{diag}\,\tau_{\mathrm{MF}}^{\mathrm{OR}}(\vartheta) \neq \tau_{\mathrm{MF}}^{\mathrm{OR}}(\vartheta, \varphi)$.

In Fig. 4(a), we observe the following trend. At small Q, lower temperatures (solid-light green) correspond to greater work extraction potential. Notably, we find the opposite behavior at increasing coupling strengths, where higher temperatures (solid-dark green) lead to a greater potential, as implied by the intersection of the two curves. In Fig. 4(b), we show $\mathcal{W}$ as a function of temperature $k_{\mathrm{B}}T/\hbar\omega_{\mathrm{L}}$ for two
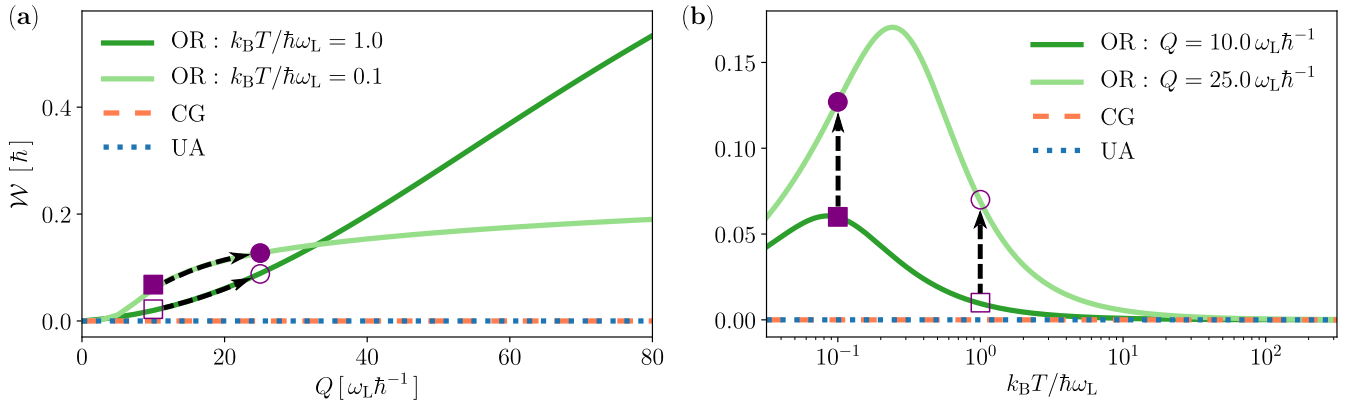
FIG. 4. Work extraction potential for different crystal symmetries. (a) $\mathcal{W}$ for the orthorhombic crystal symmetry as a function of the reorganization energy Q, for two different temperatures (solid-green lines). For the cubic (orange dashed) and uniaxial (blue dotted) symmetry one has $\mathcal{W} = 0$, due to missing energy-shell inhomogeneities. (b) Same as (a) but now shown over temperature T, for two values of Q (solid-green lines). At a fixed coupling strength, there exists an optimal temperature, at which the work extraction is maximized (e.g., if $Q = 25\,\omega_{\mathrm{L}}\hbar^{-1}$ the maximal work can be extracted at a temperature of $k_{\mathrm{B}}T/\hbar\omega_{\mathrm{L}} \approx 0.3$). This shows that the trade-off between the temperature and the coupling strength is nontrivial. The purple filled (unfilled) squares and circles are plotted for easier comparison between (a) and (b). Mind the semi-logarithmic scaling in the right figure. All other parameters are the same as in Fig. 2.

coupling strengths $Q = 10.0\,\omega_{\mathrm{L}}\hbar^{-1}$ (solid-dark green) and $Q = 25.0\,\omega_{\mathrm{L}}\hbar^{-1}$ (solid-light green). For low temperatures the limit of Eq. (12) is $\lim_{\beta \to \infty} \mathcal{W} = 0$. Likewise one has $\lim_{\beta \to 0} \mathcal{W} = 0$ because mean force corrections become less pronounced at higher temperatures [14,16] and thus energy-shell inhomogeneities vanish in the $\beta \to 0$ limit. This implies the existence of a maximum of the work extraction potential $\mathcal{W}$ at an intermediate temperature. That is, there is a trade-off between the reorganization energy and the bare thermal energy.

We conclude that some bath symmetries induce energy-shell inhomogeneities in the CMF state that can be linked to a work extraction potential $\mathcal{W}$. But we highlight that *not all* anisotropic baths generate such inhomogeneities.

VI. CONCLUSIONS

In this paper, we showed that anisotropic three-dimensional baths acting on a classical spin vector **S** substantially modify its equilibrium state, the mean force state. Such baths arise whenever a spin is embedded in crystal lattices of varying symmetries, such as the orthorhombic or monoclinic symmetry. In addition to evaluating the mean force states directly, we numerically solved the system's steady state, demonstrating convergence to the mean force state.

Secondly, we identified the presence of a spin-alignment transition in the classical spin-boson model. This is reminiscent of the well-known quantum phase transition, i.e., a change of the ground state at zero temperature, in the quantum spin-boson model. In the classical case, we find that the bath symmetry determines whether this transition occurs smoothly (monoclinic) or abruptly (orthorhombic).

Thirdly, we demonstrated how inhomogeneous distributions of a classical open spin system, i.e., "classical coherences," lead to the presence of a thermodynamic work extraction potential, equivalent to their quantum counterpart. Here, the inhomogeneous nature of the CMF state is solely

determined by the crystal symmetry. The upper limit of the work extraction potential depends on the coupling strength Q and the bath temperature T.

Understanding the impact of the symmetry of the surrounding environment is crucial to predict the equilibrium state of certain systems of interest. Examples of such systems include magnetic materials, such as thin cobalt films, where significantly different inertial spin dynamics have recently been observed for different crystal symmetries [58]. The presented results will also be relevant for the modeling of biological systems in highly complex environments [39], such as photosynthesis [39,59].

APPENDIX A: DERIVATION OF THE CLASSICAL MEAN FORCE STATE

1. Classical spin trace

The coordinates of a spin in a spherical coordinate system are given as $(S_x, S_y, S_z) = (S_0 \sin\vartheta \cos\varphi, S_0 \sin\vartheta \sin\varphi, S_0 \cos\vartheta)$ with $\vartheta \in [0, \pi]$, $\varphi \in [0, 2\pi)$, and a vector length of S_0. The trace of a function $A(S_x, S_y, S_z)$ is

$$\mathrm{tr}_S^{\mathrm{cl}}[A(S_x, S_y, S_z)] = \frac{1}{4\pi} \int_0^{2\pi} d\varphi \int_0^\pi d\vartheta \, \sin\vartheta A(S_x, S_y, S_z).$$
$$(A1)$$

The definition of $\tilde{Z}_S^{\mathrm{cl}}$ follows trivially.

2. Classical bath trace

The trace over the bath degrees of freedom is calculated via a discrete version of the bath Hamiltonian $H_B = \frac{1}{2} \sum_n (\mathbf{P}_{\omega_n}^2 + \omega_n^2 \mathbf{X}_{\omega_n}^2)$. The bath partition function becomes

$$Z_B^{cl} = \prod_n \left[\int_{-\infty}^{\infty} d\mathbf{X}_{\omega_n} \int_{-\infty}^{\infty} d\mathbf{P}_{\omega_n} e^{-\frac{1}{2}\beta \left(\mathbf{P}_{\omega_n}^2 + \omega_n^2 \mathbf{X}_{\omega_n}^2 \right)} \right]. \quad \text{(A2)}$$

3. Mean force state

Following Ref. [16], the mean force in the three-dimensional setting is calculated via the discretise bath degrees of freedom [see Eq. (A 2)], such that H_{tot} becomes

$$H_{tot} = H_S + \sum_{n=0}^{\infty} \left[\frac{1}{2} \left(\mathbf{P}_{\omega_n}^2 + \omega_n^2 \mathbf{X}_{\omega_n}^2 \right) - \mathbf{S} C_{\omega_n} \mathbf{X}_{\omega_n} \right]. \quad \text{(A3)}$$

We can simplify the integration over the bath degrees of freedom [see Eq. (A2)], by completing the square, via $\mu_n = \mathbf{S} C_{\omega_n}$,

$$H_{tot} = H_S + \sum_{n=0}^{\infty} \left[\frac{1}{2} \left[\mathbf{P}_{\omega_n}^2 + \omega_n^2 \left(\mathbf{X}_{\omega_n} - \frac{\mu_{\omega_n}}{\omega_n^2} \right)^2 \right] - \frac{\mu_{\omega_n}^2}{2\omega_n^2} \right]. \quad \text{(A4)}$$

The classical system-bath partition function is

$$Z_{SB}^{cl} = \int_0^{2\pi} d\varphi \int_0^{\pi} d\vartheta \sin\vartheta \, e^{-\beta H_{eff}} Z_B^{cl}, \quad \text{(A5)}$$

whereby we define the effective Hamiltonian as

$$H_{eff} = H_S - Q\tilde{S}^2. \quad \text{(A6)}$$

The reorganization energy Q and $\tilde{S}$ are defined in the main text (see Sec. II). This yields the partition function of the system

$$\tilde{Z}_S^{cl} = \frac{Z_{SB}^{cl}}{Z_B^{cl}} = \int_0^{2\pi} d\varphi \int_0^{\pi} d\vartheta \sin\vartheta \, e^{-\beta H_{eff}}, \quad \text{(A7)}$$

and additionally the mean force state of the three-dimensional spin-boson system,

$$\tau_{MF} = \frac{1}{\tilde{Z}_S^{cl}} e^{-\beta H_{eff}}. \quad \text{(A8)}$$

4. Classical expectation values

The expectation value is defined by $\langle S_i \rangle = \int d\Omega \, S_i \, \tau_{MF}$, with $d\Omega = \sin\vartheta \, d\vartheta \, d\varphi$ and $i \in (x, y, z)$. We normalize the expectation value with respect to the spin length, i.e., $\langle s_i \rangle = \langle S_i \rangle / S_0$, such that

$$\langle s_x \rangle = \frac{1}{\tilde{Z}_S^{cl}} \int_0^{2\pi} d\varphi \cos\varphi \int_0^{\pi} d\vartheta \sin^2\vartheta \, e^{[-\beta H_{eff}(\vartheta,\varphi)]}, \quad \text{(A9)}$$

$$\langle s_y \rangle = \frac{1}{\tilde{Z}_S^{cl}} \int_0^{2\pi} d\varphi \sin\varphi \int_0^{\pi} d\vartheta \sin^2\vartheta \, e^{[-\beta H_{eff}(\vartheta,\varphi)]}, \quad \text{(A10)}$$

$$\langle s_z \rangle = \frac{1}{\tilde{Z}_S^{cl}} \int_0^{2\pi} d\varphi \int_0^{\pi} d\vartheta \sin\vartheta \cos\vartheta \, e^{[-\beta H_{eff}(\vartheta,\varphi)]}. \quad \text{(A11)}$$

APPENDIX B: BUMPY EXPECTATION VALUE VS TEMPERATURE PLOT

As mentioned in the main text, at large system-bath coupling the magnetization is maximized above the $T \to 0\,\text{K}$
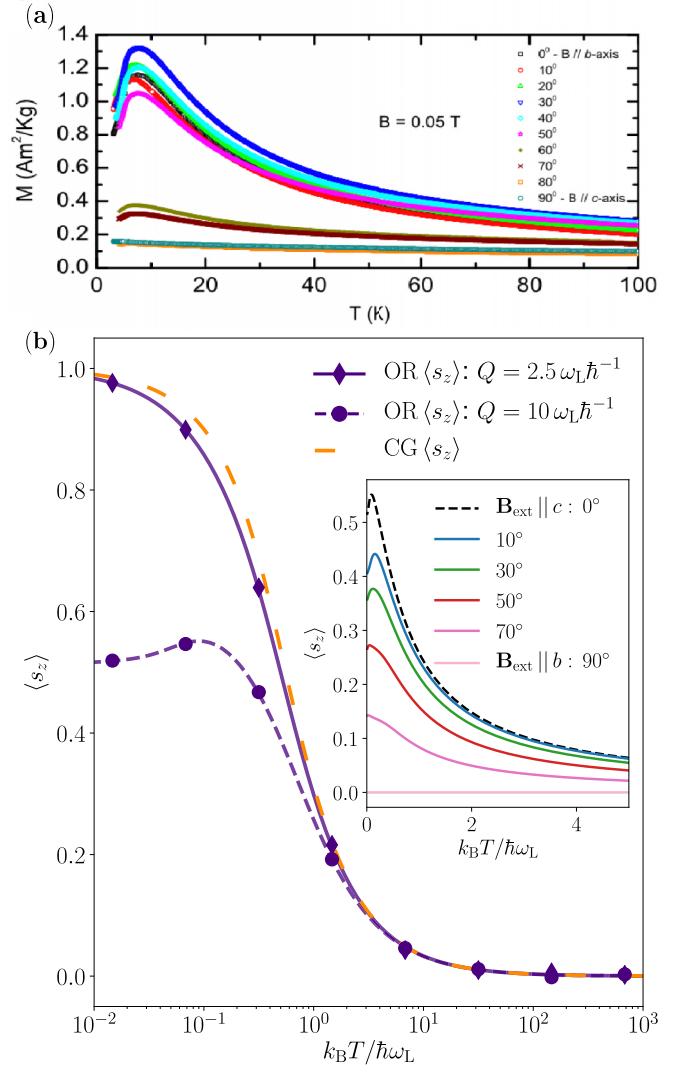

FIG. 5. Bumpy expectation value. (a) DC magnetization measurements were conducted by Pękała *et al.* [18] for a single crystal orthorhombic DyMnO$_3$. The figure shows the temperature dependence of the magnetization for different magnetic field orientations. (Figure taken from Ref. [18].) (b) Our calculated expectation value of the orthorhombic (OR) CMF state [Eq. (6)] at two different coupling strengths $Q = 2.5 \, \omega_L \hbar^{-1}$ and $Q = 10.0 \, \omega_L \hbar^{-1}$. At strong reorganization energies the expectation value reaches a maximum far above zero temperature (e.g., at $Q = 10.0 \, \omega_L \hbar^{-1}$ the maximal magnetization is at $k_B T / \hbar \omega_L \approx 0.1$). The inset shows the expectation value for different magnetic field orientations, similar to the experiment shown in (a).

limit. We show the bumpy expectation value in Fig. 5(b). In addition, we simulate the CSS via Refs. [47,49], which reproduces the bumpy expectation value [see Fig. 5(b)]. The bump directly results from the anisotropy of the bath. In fact, there is a competition between the energy term of the system H_S and the mean force correction term $Q\tilde{S}^2$. The external magnetic field tries to align the spin in its direction, whereas the correction term has other preferred directions. In the low-temperature range the environment overcomes the system energy and reduces the expectation value $\langle s_z \rangle$ to a value below its maximum. We encounter this bumpy behavior solely for
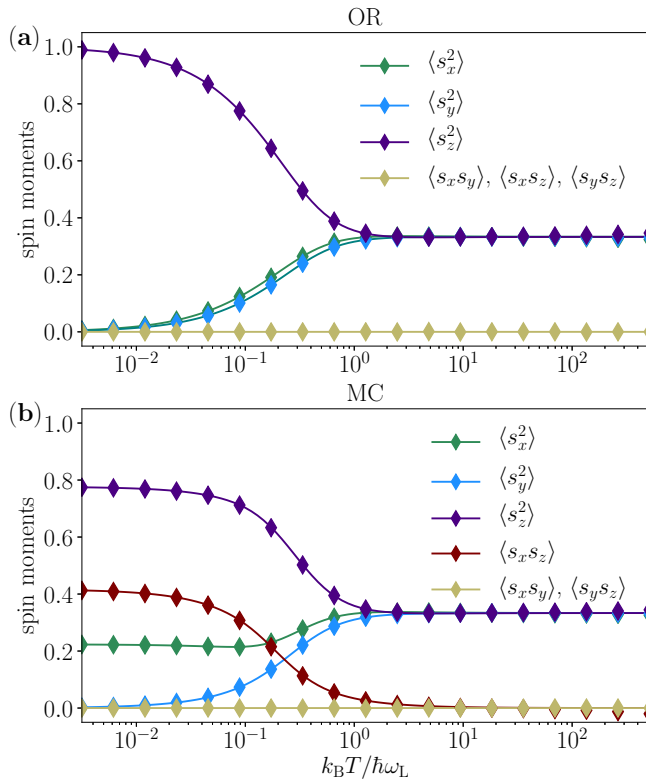
FIG. 6. Second moments for different crystal symmetries. (a) For the orthorhombic symmetry the second moments of the x and y spin component are different, i.e., $\langle s_x^2 \rangle \neq \langle s_y^2 \rangle$ (solid-green line and solid-blue line, respectively), for a certain temperature range. (b) The monoclinic CMF state shows richer structure, such as $\langle s_x s_z \rangle > 0$ (solid-red line) and $\langle s_x^2 \rangle \neq 0$ (solid-green line) at low temperatures. The higher moments of the CMF and the CSS do match for the cubic (not shown), orthorhombic, and monoclinic symmetry. The parameters are $k_B T = \hbar\omega_L$, $Q = 2.5\,\omega_L\hbar^{-1}$, and a spin length of $S_0 = \hbar$.

the orthorhombic symmetry and for a coupling tensor (9), where $c_{12} \neq 0$ and c_{11}, c_{22}, c_{33} are as in the orthorhombic case.

As we have pointed out in the main text, similar magnetization curves are observed in experiments [18–21,23]. Here we show the temperature-dependent magnetization measurements from Ref. [18] [see Fig. 5(a)] for an orthorhombic DyMnO$_3$ single crystal for different external magnetic field orientations. The inset in Fig. 5(b) shows a similar behavior of the expectation value of the orthorhombic CMF state for different external magnetic field orientations. We leave a more detailed study for future work.

APPENDIX C: HIGHER MOMENTS

The second moments of the CMF state are calculated via $\langle s_i s_j \rangle = \int_0^{2\pi} d\varphi \int_0^\pi d\vartheta\, s_i s_j \tau_{MF}(\vartheta, \varphi)$ with $i, j = x, y, z$. In Fig. 6, we show the agreement between the mean force (solid lines) and the steady-state (markers) moments. One can easily show that in the high-temperature limit, i.e., $\beta \to 0$, $\langle s_x^2 \rangle = \langle s_y^2 \rangle = \langle s_z^2 \rangle = 1/3$ for any crystal symmetry, leading to

a large variance of $\mathrm{var}(s_i) = \langle s_i^2 \rangle - \langle s_i \rangle^2 = 1/3$. In the low-temperature limit, i.e., $\beta \to \infty$, the spin is perfectly aligned along its equilibrium position such that $\langle s_i^2 \rangle = \langle s_i \rangle^2$ resulting in $\mathrm{var}(s_i) = 0$.

To conclude, we found that first-order spin expectation values, as well as higher-order expectation values, that are calculated with either the dynamical CSS or the CMF state, all match. This evidences the equality of the CSS and CMF states.

APPENDIX D: INHOMOGENEITIES

The orthorhombic CMF state is

$$\tau_{MF}^{OR}(\vartheta, \varphi) = \frac{1}{\bar{Z}_S^{cl}} e^{-\beta\left(H_S - QS_0^2\left((c_{11}\cos^2\varphi + c_{22}\sin^2\varphi)\sin^2\vartheta + c_{33}\cos^2\vartheta\right)\right)},$$

$$(D1)$$

with $c_{11} \neq c_{22} \neq c_{33}$. Following Ref. [17], we have to calculate $\eta(E) = \int d\Omega\, \tau_{MF}\delta(E - H_S(\vartheta))$. It is helpful to consider the following integral identity:

$$\int_0^{2\pi} d\varphi \exp(a\cos^2\varphi) = 2\pi e^{a/2} I_0\left(\frac{a}{2}\right), \qquad (D2)$$

where I_0 is the modified Bessel function of first kind. Using $\cos^2\varphi + \sin^2\varphi = 1$, we can rewrite Eq. (D1) and identify the parameter $a = \beta Q S_0^2 \sin^2\vartheta(c_{11} - c_{22})$, such that

$$\eta(E) = \frac{2\pi}{\bar{Z}_S^{cl}} \int_0^\pi d\vartheta \sin\vartheta\, I_0\left(\frac{a}{2}\right)\delta(E - H_S(\vartheta))$$

$$\times e^{\left[\beta\omega_L S_0 \cos\vartheta + \frac{1}{2}\beta Q S_0^2 \sin^2\vartheta(c_{11}+c_{22}) + \beta Q c_{33}\cos^2\vartheta\right]}. \quad (D3)$$

The ϑ integration is straightforward due to $\delta(E - H_S(\vartheta))$. With the substitutions $u = \omega_L S_0 \cos\vartheta$, $du = -\omega_L S_0 \sin\vartheta\, d\vartheta$, and the properties of the delta function, Eq. (D3) is

$$\eta(E) = \frac{2\pi}{\bar{Z}_S^{cl}} \frac{1}{\omega_L S_0} e^{\left[-\beta E + \beta Q\omega_L^{-2}\left(\frac{1}{2}(1-E^2)(c_{11}+c_{22}) + c_{33}E^2\right)\right]}$$

$$\times \Theta(\omega_L S_0 + E)\Theta(\omega_L S_0 - E)$$

$$\times I_0\left(\frac{1}{2}\beta Q\omega_L^{-2}(c_{11} - c_{22})(1 - E^2)\right), \quad (D4)$$

where $\Theta(\cdot)$ is the step function. The classical microcanonical density $\omega_E(\vartheta)$ is [17]

$$\omega_E(\vartheta) = \frac{\omega_L S_0}{2\pi} \frac{\delta(E - H_S(\vartheta))}{\Theta(\omega_L S_0 + E)\Theta(\omega_L S_0 - E)}. \quad (D5)$$

The homogeneous phase space distribution $\mathrm{diag}\,\tau_{MF}^{OR}(\vartheta)$ is defined as $\mathrm{diag}\,\tau_{MF}^{OR}(\vartheta) = \int dE\, \eta(E)\omega_E(\vartheta, \varphi)$ (see Ref. [17]). This leads to

$$\mathrm{diag}\,\tau_{MF}^{OR}(\vartheta) = \frac{1}{\bar{Z}_S^{cl}} I_0\left(\frac{a}{2}\right)$$

$$\times e^{\left[-\beta\left(H_S - \frac{1}{2}QS_0^2\sin^2\vartheta(c_{11}+c_{22}) - QS_0^2 c_{33}\cos^2\vartheta\right)\right]}. \quad (D6)$$

We observe that $\mathrm{diag}\,\tau_{MF}^{OR}(\vartheta, \varphi) \neq \tau_{MF}^{OR}(\vartheta)$, therefore by Eq. (12), $\mathcal{W} \geqslant 0$.

[1] C. Jarzynski, Nonequilibrium work theorem for a system strongly coupled to a thermal environment, J. Stat. Mech.: Theory Exp. (2004) P09005.

[2] U. Seifert, First and Second Law of Thermodynamics at Strong Coupling, Phys. Rev. Lett. **116**, 020601 (2016).

[3] C. Jarzynski, Stochastic and Macroscopic Thermodynamics of Strongly Coupled Systems, Phys. Rev. X **7**, 011008 (2017).

[4] P. Strasberg and M. Esposito, Stochastic thermodynamics in the strong coupling regime: An unambiguous approach based on coarse graining, Phys. Rev. E **95**, 062101 (2017).

[5] P. Talkner and P. Hänggi, Colloquium: Statistical mechanics and thermodynamics at strong coupling: Quantum and classical, Rev. Mod. Phys. **92**, 041002 (2020).

[6] H. J. D. Miller and J. Anders, Entropy production and time asymmetry in the presence of strong interactions, Phys. Rev. E **95**, 062123 (2017).

[7] E. Aurell, Unified picture of strong-coupling stochastic thermodynamics and time reversals, Phys. Rev. E **97**, 042112 (2018).

[8] A. Trushechkin, Quantum master equations and steady states for the ultrastrong-coupling limit and the strong-decoherence limit, Phys. Rev. A **106**, 042209 (2022).

[9] J. Thingna, J.-S. Wang, and P. Hänggi, Generalized Gibbs state with modified Redfield solution: Exact agreement up to second order, J. Chem. Phys. **136**, 194110 (2012).

[10] M. Campisi, P. Talkner, and P. Hänggi, Thermodynamics and fluctuation theorems for a strongly coupled open quantum system: An exactly solvable case, J. Phys. A: Math. Theor. **42**, 392002 (2009).

[11] A. S. Trushechkin, M. Merkli, J. D. Cresser, and J. Anders, Open quantum system dynamics and the mean force Gibbs state, AVS Quantum Sci. **4**, 012301 (2022).

[12] F. Binder, L. A. Correa, C. Gogolin, J. Anders, and G. Adesso, eds., *Thermodynamics in the Quantum Regime: Fundamental Aspects and New Directions*, Fundamental Theories of Physics, Vol. 195 (Springer International Publishing, Cham, 2018).

[13] Y.-F. Chiu, A. Strathearn, and J. Keeling, Numerical evaluation and robustness of the quantum mean-force Gibbs state, Phys. Rev. A **106**, 012204 (2022).

[14] J. D. Cresser and J. Anders, Weak and Ultrastrong Coupling Limits of the Quantum Mean Force Gibbs State, Phys. Rev. Lett. **127**, 250601 (2021).

[15] N. Anto-Sztrikacs, A. Nazir, and D. Segal, Effective-Hamiltonian theory of open quantum systems at strong coupling, PRX Quantum **4**, 020307 (2023).

[16] F. Cerisola, M. Berritta, S. Scali, S. A. R. Horsley, J. D. Cresser, and J. Anders, Quantum-classical correspondence in spin-boson equilibrium states at arbitrary coupling, arXiv:2204.10874.

[17] A. Smith, K. Sinha, and C. Jarzynski, Quantum coherences and classical inhomogeneities as equivalent thermodynamics resources, Entropy **24**, 474 (2022).

[18] M. Pękała, F. Wolff-Fabris, J.-F. Fagnard, Ph. Vanderbemden, J. Mucha, M. M. Gospodinov, V. Lovchinov, and M. Ausloos, Magnetic properties and anisotropy of orthorhombic DyMnO$_3$ single crystal, J. Magn. Magn. Mater. **335**, 46 (2013).

[19] S. Harikrishnan, S. Rößler, C. M. N. Kumar, H. L. Bhat, U. K. Rößler, S. Wirth, F. Steglich, and S. Elizabeth, Phase transitions and rare-earth magnetism in hexagonal and orthorhombic DyMnO$_3$ single crystals, J. Phys.: Condens. Matter **21**, 096002 (2009).

[20] K. Bhoi, T. Dam, S. R. Mohapatra, M. M. Patidar, D. Singh, A. K. Singh, P. N. Vishwakarma, P. D. Babu, V. Siruguri, and D. K. Pradhan, Studies of magnetic phase transitions in orthorhombic DyMnO$_3$ ceramics prepared by acrylamide polymer gel template method, J. Magn. Magn. Mater. **480**, 138 (2019).

[21] A. N. Bogdanov, A. V. Zhuravlev, and U. K. Rößler, Spin-flop transition in uniaxial antiferromagnets: Magnetic phases, reorientation effects, and multidomain states, Phys. Rev. B **75**, 094425 (2007).

[22] N. O. Antropov, E. A. Kravtsov, M. V. Makarova, V. V. Proglyado, T. Keller, I. A. Subbotin, E. M. Pashaev, G. V. Prutskov, A. L. Vasiliev, Yu. M. Chesnokov, N. G. Bebenin, M. A. Milyaev, V. V. Ustinov, B. Keimer, and Yu. N. Khaydukov, Tunable spin-flop transition in artificial ferrimagnets, Phys. Rev. B **104**, 054414 (2021).

[23] B. Biswas, V. F. Michel, Ø. S. Fjellvåg, G. Bimashofer, M. Döbeli, M. Jambor, L. Keller, E. Müller, V. Ukleev, E. V. Pomjakushina, D. Singh, U. Stuhr, C. A. F. Vaz, T. Lippert, and C. W. Schneider, Role of Dy on the magnetic properties of orthorhombic DyFeO$_3$, Phys. Rev. Mater. **6**, 074401 (2022).

[24] S. K. Srivastava, Magnetic property of Mn-doped monoclinic ZrO$_2$ compounds, J. Supercond. Nov. Magn. **33**, 2501 (2020).

[25] G. Long, H. Zhang, D. Li, R. Sabirianov, Z. Zhang, and H. Zeng, Magnetic anisotropy and coercivity of Fe$_3$Se$_4$ nanostructures, Appl. Phys. Lett. **99**, 202103 (2011).

[26] H. Zhang, G. Long, D. Li, R. Sabirianov, and H. Zeng, Fe$_3$Se$_4$ Nanostructures with giant coercivity synthesized by solution chemistry, Chem. Mater. **23**, 3769 (2011).

[27] D. Singh, S. K. Gupta, H. He, and Y. Sonvane, First-principles study of the electronic, magnetic and optical properties of Fe$_3$Se$_4$ in its monoclinic phase, J. Magn. Magn. Mater. **498**, 166157 (2020).

[28] F. B. Anders, R. Bulla, and M. Vojta, Equilibrium and Nonequilibrium Dynamics of the Sub-Ohmic Spin-Boson Model, Phys. Rev. Lett. **98**, 210402 (2007).

[29] A. Alvermann and H. Fehske, Sparse Polynomial Space Approach to Dissipative Quantum Systems: Application to the Sub-Ohmic Spin-Boson Model, Phys. Rev. Lett. **102**, 150601 (2009).

[30] S. Florens, D. Venturelli, and R. Narayanan, Quantum phase transition in the spin boson model, in *Quantum Quenching, Annealing and Computation* (Springer, Berlin, Heidelberg, 2010), pp. 145–162.

[31] G. De Filippis, A. de Candia, L. M. Cangemi, M. Sassetti, R. Fazio, and V. Cataudella, Quantum phase transitions in the spin-boson model: Monte Carlo method versus variational approach a la Feynman, Phys. Rev. B **101**, 180408(R) (2020).

[32] Y.-Z. Wang, S. He, L. Duan, and Q.-H. Chen, Quantum phase transitions in the spin-boson model without the counterrotating terms, Phys. Rev. B **100**, 115106 (2019).

[33] A. J. Leggett, S. Chakravarty, A. T. Dorsey, M. P. A. Fisher, A. Garg, and W. Zwerger, Dynamics of the dissipative two-state system, Rev. Mod. Phys. **59**, 1 (1987).

[34] U. Weiss, *Quantum Dissipative Systems* (World Scientific, Singapore, 1999).

[35] L. Ferialdi, Exact non-Markovian master equation for the spin-boson and Jaynes-Cummings models, Phys. Rev. A **95**, 020101(R) (2017).

[36] P. L. Orman and R. Kawai, A qubit strongly interacting with a bosonic environment: Geometry of thermal states, arXiv:2010.09201.

[37] S. Lloyd, Quantum coherence in biological systems, J. Phys.: Conf. Ser. **302**, 012037 (2011).

[38] A. Kolli, E. J. O'Reilly, G. D. Scholes, and A. Olaya-Castro, The fundamental role of quantized vibrations in coherent light harvesting by cryptophyte algae, J. Chem. Phys. **137**, 174109 (2012).

[39] S. Huelga and M. Plenio, Vibrations, quanta and biology, Contemp. Phys. **54**, 181 (2013).

[40] M. Arndt, T. Juffmann, and V. Vedral, Quantum physics meets biology, HFSP J. **3**, 386 (2009).

[41] S. Dattagupta, Spin-boson model of quantum dissipation in graphene: Nonlinear electrical response, Phys. Rev. B **104**, 085411 (2021).

[42] C. Wang, J. Ren, and J. Cao, Unifying quantum heat transfer in a nonequilibrium spin-boson model with full counting statistics, Phys. Rev. A **95**, 023610 (2017).

[43] Y.-Y. Zhang, Q.-H. Chen, and K.-L. Wang, Quantum phase transition in the sub-Ohmic spin-boson model: An extended coherent-state approach, Phys. Rev. B **81**, 121105(R) (2010).

[44] D. Dzsotjan, A. S. Sørensen, and M. Fleischhauer, Quantum emitters coupled to surface plasmons of a nanowire: A Green's function approach, Phys. Rev. B **82**, 075427 (2010).

[45] S. Nemati, C. Henkel, and J. Anders, Coupling function from bath density of states, Europhys. Lett. **139**, 36002 (2022).

[46] T. G. Philbin and S. A. R. Horsley, Damping the zero-point energy of a harmonic oscillator, arXiv:1304.0977.

[47] J. Anders, C. R. J. Sait, and S. A. R. Horsley, Quantum Brownian motion for magnets, New J. Phys. **24**, 033020 (2022).

[48] T. Mori and S. Miyashita, Dynamics of the density matrix in contact with a thermal bath and the quantum master equation, J. Phys. Soc. Jpn. **77**, 124005 (2008).

[49] S. Scali, S. Horsley, J. Anders, and F. Cerisola, Spidy.jl—Open-source Julia package for the study of non-Markovian stochastic dynamics, arXiv:2310.03008.

[50] F. E. Neumann and O. E. Meyer, *Vorlesungen über die theorie der elastizität der festen Körper und des Lichtäthers* (B.G. Teubner, Leipzig, 1885), https://archive.org/details/vorlesungenberd01neumgoog/mode/2up.

[51] S. Haussüh, *Physical Properties of Crystals-An Introduction* (WILEY-VCH, Weinheim, 2007).

[52] C. Malgrange, C. Ricolleau, and M. Schlenker, *Symmetry and Physical Properties of Crystals* (Springer Netherlands, Dordrecht, 2014).

[53] R. E. Newnham, *Properties of Materials: Anisotropy, Symmetry, Structure* (Oxford University Press, Oxford, 2005).

[54] C. R. Hogg, F. Cerisola, J. D. Cresser, S. A. R. Horsley, and J. Anders, Enhanced entanglement in multi-bath spin-boson models, arXiv:2306.11036.

[55] N. Zhou, L. Chen, D. Xu, V. Chernyak, and Y. Zhao, Symmetry and the critical phase of the two-bath spin-boson model: Ground-state properties, Phys. Rev. B **91**, 195129 (2015).

[56] M. Xu, Y. Yan, Q. Shi, J. Ankerhold, and J. T. Stockburger, Taming Quantum Noise for Efficient Low Temperature Simulations of Open Quantum Systems, Phys. Rev. Lett. **129**, 230601 (2022).

[57] P. Kammerlander and J. Anders, Coherence and measurement in quantum thermodynamics, Sci. Rep. **6**, 22174 (2016).

[58] V. Unikandanunni, R. Medapalli, M. Asa, E. Albisetti, D. Petti, R. Bertacco, E. E. Fullerton, and S. Bonetti, Inertial Spin Dynamics in Epitaxial Cobalt Films, Phys. Rev. Lett. **129**, 237201 (2022).

[59] A. Trushechkin, Calculation of coherences in Förster and modified Redfield theories of excitation energy transfer, J. Chem. Phys. **151**, 074101 (2019).